Bacterial crystalline cellulose secretion via a supramolecular BcsHD scaffold

Wiem Abidi, Marion Decossas, Lucia Torres-Sanchez, Lucie Puygrenier, Sylvie Letoffe, Jean-Marc Ghigo, Petya V. Krasteva

MICROBIOLOGY

Bacterial crystalline cellulose secretion via a supramolecular BcsHD scaffold

Wiem Abidi[1,2,3]†, Marion Decossas[1,2]†, Lucía Torres-Sánchez[1,2,3]†, Lucie Puygrenier[2], Sylvie Létoffé[4], Jean-Marc Ghigo[4], Petya V. Krasteva[1,2]*

Cellulose, the most abundant biopolymer on Earth, is not only the predominant constituent of plants but also a key extracellular polysaccharide in the biofilms of many bacterial species. Depending on the producers, chemical modifications, and three-dimensional assemblies, bacterial cellulose (BC) can present diverse degrees of crystallinity. Highly ordered, or crystalline, cellulose presents great economical relevance due to its ever-growing number of biotechnological applications. Even if some acetic acid bacteria have long been identified as BC superproducers, the molecular mechanisms determining the secretion of crystalline versus amorphous cellulose remain largely unknown. Here, we present structural and mechanistic insights into the role of the accessory subunits BcsH (CcpAx) and BcsD (CesD) that determine crystalline BC secretion in the *Gluconacetobacter* lineage. We show that oligomeric BcsH drives the assembly of BcsD into a supramolecular cytoskeletal scaffold that likely stabilizes the cellulose-extruding synthase nanoarrays through an unexpected inside-out mechanism for secretion system assembly.

INTRODUCTION

Cellulose is an unbranched homopolymer of β-1,4–linked D-glucose moieties, which represents more than half of the world's organic carbon. Although most of the polysaccharide is synthesized as a component of the plant cell wall, it is also used as many bacterial species as an important building component of their biofilm matrix. It can provide fitness and survival advantages in the environment and also partake in important host-pathogens interactions in both symbiotic and pathogenic species. In some bacteria, such as representatives of the *Gluconacetobacter* lineage, secreted crystalline polymers can also serve as bona fide motility organelles to propel the cells onto a solid substrate or float the aerobic bacteria to oxygen-rich air-liquid interfaces.

While bacterial cellulose (BC) was first described at the end of the 19th century, it was not until the end of the 20th that biochemical studies on the *Gluconacetobacter xylinus* cellulose synthase led to the identification of cyclic diguanylate (c-di-GMP) as its allosteric activator (*1*). With the revolution of DNA sequencing and genome assemblies in the beginning of the 21st century, c-di-GMP–metabolizing enzymes were discovered in most characterized bacterial species and the cyclic dinucleotide revealed itself as a master regulator of bacterial biofilm formation, often through direct control not only of cellulose secretion but also of other functionally similar albeit structurally diverse synthase-dependent systems for exopolysaccharide secretion (*2*, *3*).

It is now well established that BC can be produced by several distinct types of cellulose secretion systems, the classification of which depends both on the type of involved Bcs (BC synthesis) subunits and the physicochemical characteristics of the secreted polysaccharide (*4*, *5*). In most bacterial systems, cellulose biogenesis is dependent on a conserved BcsAB protein tandem, and a string of detailed structural works over the past decade have provided minute details of how the BcsB-assisted synthase BcsA senses c-di-GMP to simultaneously polymerize its substrate and extrude the growing polysaccharide across the inner bacterial membrane (*5*, *6*).

In addition to the BcsAB tandem, most cellulose secretion operons encode a variety of accessory Bcs subunits, many of which are indispensable for cellulose secretion. The past few years greatly improved our understanding of the enzymatic details surrounding glucose polymerization and allowed us to better place these secretion systems in the big picture of bacterial signaling, secretion systems expression and assembly, biofilm formation and host colonization, as well as structural and functional evolution from the bacterial to the eukaryotic domains of life.

Examples include the detailed structural and functional characterization of physiologically important Bcs components [e.g., the crystallinity factor BcsD (*7*), the outer membrane secretin BcsC (*8*), or the phosphoethanolamine (pEtN) transferase BcsG (*9*)], the discovery of various covalent modifications of the polysaccharide that can effectively turn it into an adhesive glue for host tissue colonization [e.g., cellulose acetylation (*10*) or pEtN modification (*11*)], the assembly of multicomponent Bcs secretion machineries that determine the subcellular targeting of the system, as well as provide for synthase-proximal c-di-GMP retention (*5*, *12*, *13*), the formation of supramolecular cytoskeletal assemblies associated with synthase nanoarray formation for crystalline cellulose secretion (*14*), and the first detailed structural insights into plant cellulose synthases (*15*).

Despite several decades of extensive and multidisciplinary research, however, the roles of many key Bcs actors have remained unclear, whereas the need for sustainable materials for biotechnological applications keeps growing. The cellulose secreted by *Gluconacetobacter* bacteria, in particular, presents an ultrapure microcrystalline polymer that is often preferred to lignin- and hemicellulose-mixed plant-derived sources and is widely used in the

[1]Université de Bordeaux, CNRS, Bordeaux INP, CBMN, UMR 5248, Pessac, France. [2]'Structural Biology of Biofilms' Group, European Institute of Chemistry and Biology (IECB), Pessac, France. [3]Doctoral School of Therapeutic Innovation ITFA, Université Paris-Saclay, Orsay, France. [4]Institut Pasteur, Université de Paris, UMR CNRS2001, 'Genetics of Biofilms' laboratory, 25-28 rue du Docteur Roux, 75015 Paris, France.
*Corresponding author. Email: pv.krasteva@iecb.u-bordeaux.fr
†These authors contributed equally to this work.

food, cosmetics, electronics, and biomedical industries (*5*). In *Gluconacetobacter hansenii* (formerly *Acetobacter xylinum* and also known as *Komagataeibacter* or *Novacetimonas hansenii*), the Bcs secretion system is assembled as a narrow linear nanoarray of so-called terminal complexes (TCs) that positions along the long axis of the cell rod (*16*). The *bcs* genes themselves are found in three separate *bcs* clusters (fig. S1), and a recent study based on markerless chromosomal deletions of each of the corresponding synthases reported that only the *bcs1* cluster determines crystalline cellulose secretion (*17*). The BcsAB1 tandem in the model *G. hansenii* ATCC 23769 strain used here is expressed from a single gene (fig. S1), and the use of fragment-specific antibodies showed that the expressed protein is post-translationally cleaved to three polypeptides corresponding to the BcsA inner membrane and catalytic glycosyl transferase domains, the BcsA C-terminal PilZ domain–containing region, and the BcsB polypeptide (*18*). In addition, the *bcs1* cluster contains the coding regions for the outer membrane exporter BcsC, essential for secretion , which contains a large periplasmic N-terminal region with multiple tetratricopeptide repeat (TPR) scaffolding motifs and a C-terminal porin domain; for two glycan hydrolases, namely, an extracellular β-glucosidase (BglX) and a periplasmic endoglucanase (BcsZ or Cmc_{Ax}) that are necessary for optimal cellulose secretion; and for two additional proteins, disruptions of which either abolish [for BcsH (CcpAx)] or greatly decrease [for BcsD (Cmc_{Ax})] the secretion of crystalline cellulose (fig. S1).

BcsD is a small, ~17-kDa protein that has been shown to form cylinder-shaped octamers, whose lumen is separated in four independent passageways by the protruding N-terminal ends of the eight protomers and are large enough to accommodate four separate translocating oligosaccharides (*7*). This, together with very faint Western blot signals supporting periplasmic localization in cell fractionation experiments (*19*), has led to a model where the protein acts as a polysaccharide conduit downstream of the biosynthetic BcsAB tandem. This conduit would prevent aggregation between nascent cellulose chains in the periplasm, before their extrusion by the outer membrane porin BcsC. On the basis of in cellulo imaging of functional BcsD-EGFP (enhanced green fluorescent protein) protein fusions, BcsD has been found to position in a linear longitudinal array along one side of the cell, not unlike the cellulose-extruding TCs. This linear localization is dependent on the presence of BcsH (Fig. 1A), and direct interactions between the two proteins have been confirmed by protein pull-down and isothermal titration experiments (*20*). While the *bcsH* gene has been annotated to encode a 37-kDa protein, functional complementation and protein purification experiments based on alternative open reading frames within *bcsH* have suggested that BcsH is actually a small, ~8-kDa polypeptide (herein referred to as $BcsH^{CTD}$) (*20*).

Here, we set out to uncover the exact molecular mechanisms for BcsH-driven BcsD polymerization and crystalline cellulose secretion. We present nearly atomic resolution cryo–electron microscopy (cryo-EM) structures of both BcsD and BcsHD protein complexes (3.3 and 2.5 Å, respectively). While the former is in almost perfect agreement with previously reported crystallographic data (*7*), we demonstrate that, within the $BcsH^{CTD}D$ complex, $BcsH^{CTD}$ adopts at least two discrete conformations to drive BcsD into "beads-on-a-string" filamentous polymers (herein referred as cis-filamentation). We further show that, when coexpressed with BcsD, the annotated *bcsH* coding region actually expresses as a stable full-length protein ($BcsH^{FL}$, ~37 kDa), which assembles into heat- and SDS-resistant dimers, likely driving the formation of higher-order macromolecular assemblies through trans-interactions between BcsHD filaments. In addition, we show that, in situ, the BcsHD assemblies share remarkable morphological similarities with the recently discovered cortical belt, namely, an intracellular cytoskeletal element that spatially correlates with the cellulose exit sites and the assembled crystalline cellulose ribbon (CR) (*14*). Last, we detect specific protein-protein interactions between the BcsHD components and the regulatory $BcsA^{PilZ}$ module, further supporting that BcsHD can function as an intracellular three-dimensional (3D) scaffold for TC array formation and crystalline cellulose secretion.

RESULTS AND DISCUSSION

Structural insights into BcsH-driven BcsD filamentation

To determine the molecular mechanisms of the BcsD-$BcsH^{CTD}$ interaction, we proceeded to examine the solution structures of both BcsD and BcsHD protein complexes. We first recombinantly expressed and purified *G. hansenii* BcsD via a cleavable N-terminal hexahistidine tag ($Bcs^{His}D$). The purified untagged protein eluted as a single Gaussian peak from the size exclusion column, and we proceeded to solve its cryo-EM structure as an important control of the oligomeric state and conformation of the protein in solution. The structure was consistent with previous crystallographic reports (*7*) in terms of both protomer fold and the quaternary octameric structure, with overall dimensions of ~65 Å × 90 Å and a large central lumen separated into four independent passageways. Each protomer presents a four-stranded antiparallel β-sheet flanked by a four-helix bundle on one side with an overall secondary structure topology α1-α2-α3-β1-β2-α4-β3-β4. A very short, five-residue α-helix (α5), which is resolved in the crystal structures between β3 and β4 and completely solvent-exposed in the assembled octamer, is not well resolved in the cryo–electron density map and therefore omitted from the refined atomic model. The BcsD octamer features a D4 point group symmetry and can be viewed as a tetramer of head-to-head dimers in which the antiparallel β-sheets point away from each other and line the large polar entries of the central lumen, whereas the α-helical bundles, and in particular the fishhook-like arrangements of α1 and α2, interlock at the equatorial plane of the octamer. Alternatively, it can be presented as a stack of two planar tetramers that are twisted by about 50° relative to each other. Important conformational changes can be seen in the loops connecting α4 and β3, and analysis of the three crystal structures reported previously reveals that these loops indeed feature an important conformational plasticity (see below).

For expression of the BcsH-BcsD complex, we tested several different strategies for complex reconstitution or coexpression. We successfully copurified a stable $BcsH^{CTD}$-BcsD complex upon the coexpression of N-terminally tagged *G. hansenii* $BcsH^{CTD}$ ($BcsH^{isH^{CTD}}$) with untagged BcsD in *Escherichia coli*. Upon size exclusion chromatography, the purified proteins co-eluted primarily in the void volume of the gel filtration column (Fig. 1, B and C), indicating either protein aggregation or the formation of nonaggregative macromolecular species. Unexpectedly, observation of the corresponding sample by cryo-EM revealed the formation of beads-on-a-string–like linear filaments with BcsD octamers arranged in a

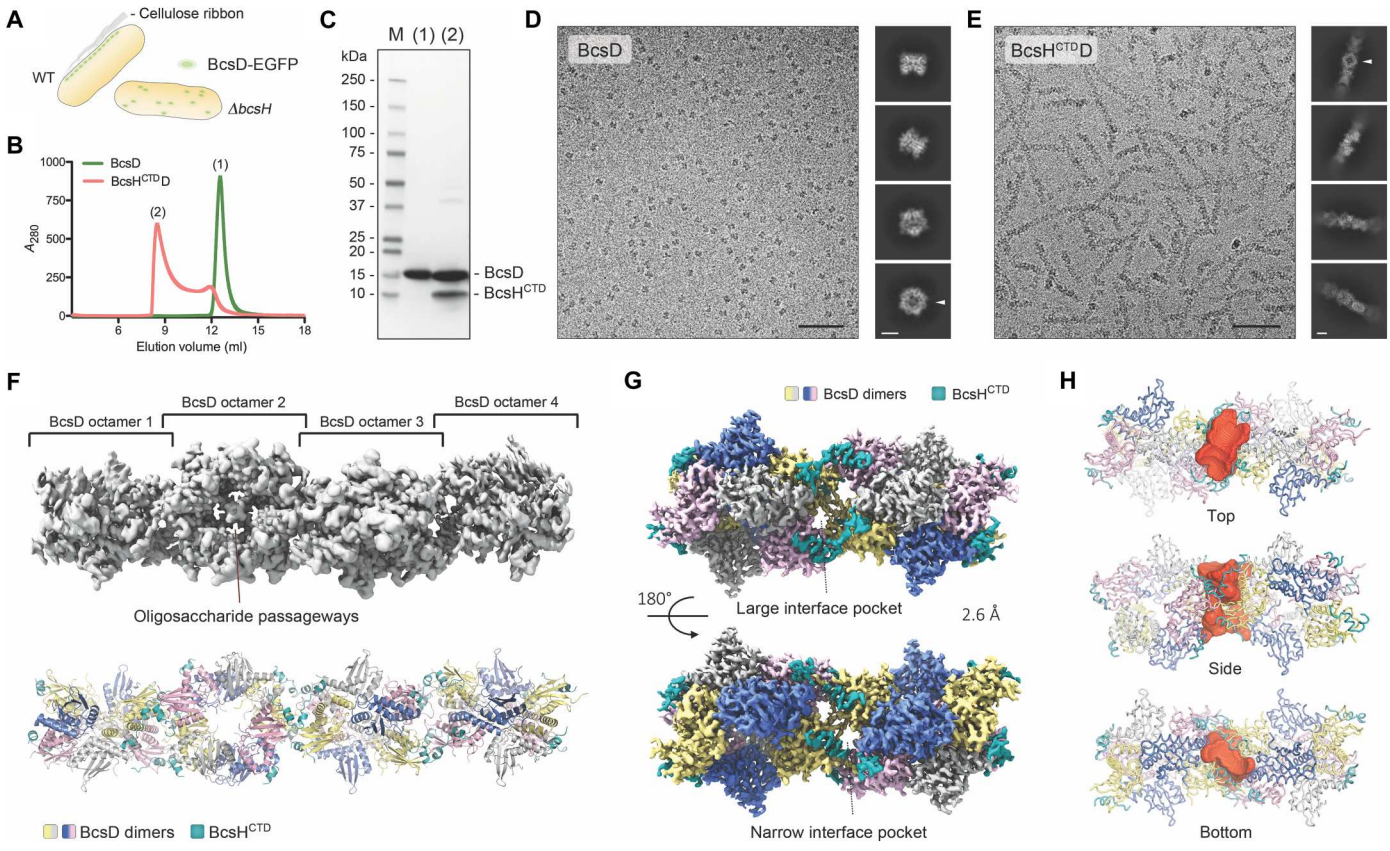

Fig. 1. BcsH-driven BcsD filamentation. (**A**) Schematic representation of BcsH-dependent BcsD localization and cellulose secretion in vivo (*5*,*20*). WT, wild type. (**B**) Size exclusion chromatography on a Superdex 200 Increase column for purified BcsD versus the BcsH^{CTD}D complex. (**C**) Coomassie-stained SDS-PAGE–migrated samples of purified BcsD alone versus BcsH^{CTD}D. (**D** and **E**) Cryo–electron micrographs and representative 2D class averages of BcsD alone versus BcsH^{CTD}D. The four central passageways in the BcsD octamers are visible in the top views as indicated by white arrowheads. Scale bars for the electron micrographs and 2D class averages are 50 and 5 nm, respectively. (**F**) Unsharpened cryo-EM map of a BcsH^{CTD}D filament showing beads-on-a-string polymerization of BcsD octamers (top) and a cartoon representation of the refined atomic model (bottom). (**G**) Sharpened locally refined electron density map of two BcsH-bound BcsD octamers. (**H**) Cartoon representation of the refined atomic model with volume visualization of the interoctamer pocket (red).

variety of orientations relative to the longitudinal axes of these macromolecular assemblies (Fig. 1, D and E). The high-resolution 3D electron density reconstruction (Fig. 1, F and G) revealed a $BcsH_4$-$BcsD_8$ stoichiometry and corroborated the lack of strict helical symmetry along the filaments.

Within the filaments, the four BcsH^{CTD} protomers adopt, in pairs, two discreet helix-linker-helix conformations to bridge adjacent BcsD octamers (Fig. 1, F to H, and fig. S2A). These alternative conformations, together with additional interactions between motifs from pairs of the interface BcsD protomers, create a C2-pseudosymmetrical cavity that features a very large, ~40 Å × 25 Å × 30 Å pocket on one side of the filament connected via two narrow conduits to a narrow twisted pocket on the other (Fig. 1, F to H, and fig. S2A). The large versus narrow cavity distribution along the filament does not follow strict periodicity, as the same planar tetramer of a given BcsD octamer can participate in the formation of either one or two large interface pockets on either side. The asymmetrical distribution and substantial size of these surface cavities can allow for the creation of microcompartments along the BcsHD filaments and perhaps allow for additional protein or small-molecule recruitment.

Despite the different BcsH^{CTD} conformations, binding of each protomer occurs via virtually identical motifs. First, a short, N-proximal α-helix plugs into an intrasubunit BcsD pocket formed between the peripheral tip of the antiparallel β-sheet and the connecting loops of the underlying α-helical bundle (Fig. 2, A to D). The interactions are highly hydrophobic with an N-proximal BcsH plug formed by residues Met^{318}, Val^{321}, Phe^{322}, and Leu^{325} (numbering according to the annotated *bcsH* open reading frame) and a number of core BcsD residues that are exposed through displacement of the α4-β3 connecting loop (Fig. 2, A to D, and fig. S3). This BcsH-BcsD interface buries around 766 Å^2 of surface area with a free energy gain of −15.7 kcal/mol per BcsH protomer. In the two BcsH subunits lining the large interface cavity, the N-terminal BcsH^{CTD} helix connects under a sharp angle with a short, two-turn helix and an extended S^{334}PRP linker that bridge the interoctamer space (Fig. 2, A to D, and fig. S2). On the other end, the polypeptide chain makes an approximately 90° turn to fold into a C-terminal helix that plugs into an intersubunit BcsD pocket formed at the bends of the N-terminal α1-α2 fishhooks of the adjacent BcsD octamer. Again, the interactions are primarily hydrophobic, with the contribution of a C-proximal BcsH hydrophobic plug formed by residues Leu^{339} and Leu^{343} (Fig. 2, A to D). This C-

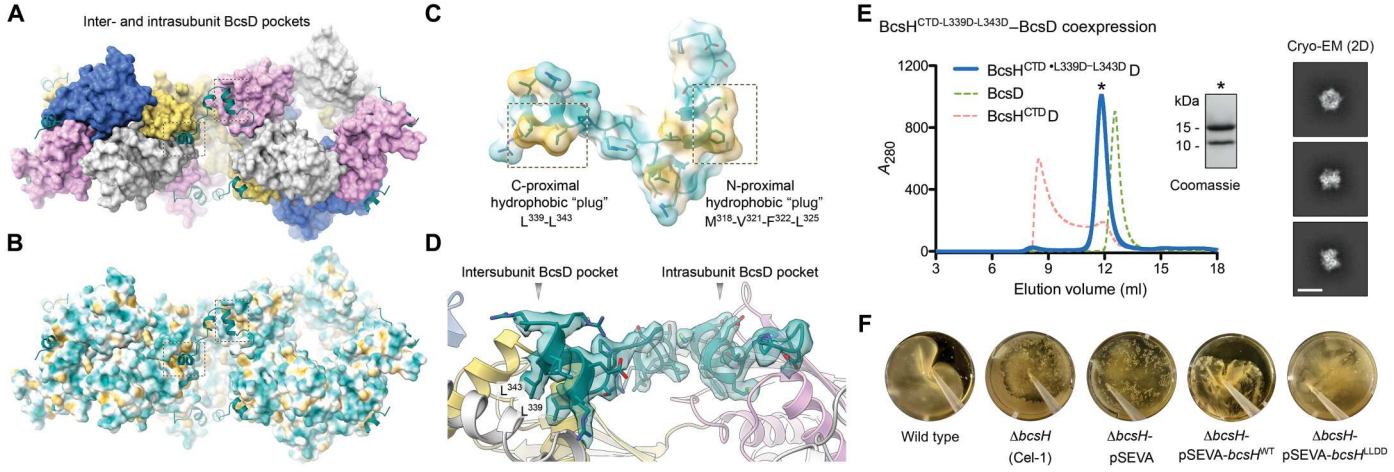

Fig. 2. BcsH-BcsD interactions and in vivo validation of the polymerization mechanism. (**A** and **B**) Inter- and intrasubunit BcsH-binding pockets on BcsD. BcsD is shown in surface representation colored by subunits (top) and surface hydrophobicity (bottom). BcsH is shown in teal, in cartoon representation. (**C**) Hydrophobicity-colored surface representation of a BcsH protomer with the N-terminal and C-terminal hydrophobic plugs annotated. (**D**) Cartoon representation of a BcsH protomer in its corresponding electron density as bound to the inter- and intrasubunit pockets on BcsD. The C-terminal hydrophobic plug residues L^{339} and L^{343} are annotated. (**E**) In vitro validation of the structure-derived polymerization mechanism. Left: Size exclusion chromatography of a purified $BcsH^{CTD•L339D-L343D}$–BcsD complex. Inset: SDS–polyacrylamide gel electrophoresis (SDS-PAGE) visualization of the peak elution fraction. Right: Represented cryo-EM 2D class averages of the peak fraction with a scale bar of 10 nm. (**F**) In vivo validation of the polymerization mechanism. Functional complementation of cellulose secretion and surface pellicle formation in the Cel-1 mutant following plasmid-based expression of wild-type versus the $L^{339}D$-$L^{343}D$ mutant BcsH. Cultures of wild-type *G. hansenii*, the Cel-1 mutant cells, and empty vector–transformed Cel-1 cells are included as controls.

terminal interface buries about 623 $Å^2$ of surface area and has a free energy gain of −7 kcal/mol, shared between the two interacting BcsD subunits. In the two BcsH protomers lining the narrow interface pocket, the interoctamer linker is not resolved in the electron density map (fig. S2); however, interactions through the C-terminal BcsH helix are virtually the same. Overall, per BcsD octamer, inter- and intrasubunit BcsH-binding interfaces are presented by eight and four BcsD protomers, respectively.

Apart from the BcsH-BcsD interactions described above, the cis-filamentation is stabilized by additional BcsD-BcsD interactions (fig. S3, A and B). In one interface BcsD protomer per octamer, the α4-β3 connecting loop is flipped further away from the tip of the antiparallel β sheet to partake into pseudosymmetric contacts across the interface cavity stabilized by π-stacking interactions between Arg^{113} from one BcsD subunit and Phe^{123} from the corresponding BcsD protomer from the adjacent octamer (fig. S3). In addition, the C terminus of each of these two BcsD subunits extends across the intersubunit cavity to engage in backbone interactions with the β sheet of a different interface BcsD protomer from the neighboring octamer (fig. S3C). Overall, these BcsD-BcsD interactions are not sufficient to drive BcsD filamentation as evidenced by the single octameric species of BcsD in solution in vitro and the lack of linear fluorescent BcsD-EGFP arrays in the absence of BcsH in vivo (*20*). Nevertheless, multiple such contacts can contribute weak interactions both in BcsHD cis-filamentation and in the formation of higher-order multimeric species, especially in crowded environments in cellulo.

It is important to note that both the BcsD-BcsD and BcsH-BcsD interactions involve residues of the α4-β3 connecting loop in the respective BcsD subunits, suggesting that the high conformational plasticity of this motif among the crystal (*7*) and cryo-EM structures (fig. S3C) is not random but rather a functionally important structural feature. The overall sequence surrounding this α4-β3 connecting loop, including the Arg^{113}-Phe^{123} tandem, is highly conserved in the *Gluconacetobacter* lineage of crystalline cellulose producers, but overall not conserved across the larger protein family of BcsD homologs. In some organisms such as the plant pathogen *Dickeya dadantii*, known for the secretion of thick cellulosic nanofibers more similar to the *Gluconacetobacter* crystalline ribbons than the *E. coli* amorphous cellulose (*21*), the Phe^{123} counterpart is a glutamate residue, which could potentially allow for salt bridge formation between BcsD octamers and contribute to the secretion of more structured polysaccharide assemblies.

To validate the BcsHD polymerization mechanism deduced from the cryo-EM structure, we reasoned that disruption of the weaker binding to the intersubunit BcsD interface will prevent cis-filamentation while preserving the ability to copurify BcsD via $BcsH^{CTD}$ binding to the intrasubunit BcsD pocket. To this end, we introduced the double $L^{339}D$-$L^{343}D$ mutation in $BcsH^{CTD}$ and coexpressed it with BcsD. As designed, the mutant BcsH variant copurified with BcsD and eluted as a single Gaussian peak upon gel filtration, consistent with the presence of individual BcsD octamers in solution (Fig. 2E). We further validated these results in functional complementation assays in the cellulose-deficient Cel-1 strain carrying a transposon knockout mutation in *bcsH* (*22*). While plasmid-based expression of full-length wild-type BcsH was able to complement the cellulose secretion defect as evidenced by the formation of a mechanically resistant surface-exposed cellulosic pellicle and limited cell sedimentation, most of the cells expressing the $L^{339}D$-$L^{343}D$ BcsH mutant were found at the bottom of the culture medium (Fig. 2F). In addition to validation of the structure-based polymerization model, these data also provided us with a tool to independently evaluate putative trans-oligomerization mechanisms as discussed below.

Formation of higher-order macromolecular structures

As mentioned above, the annotated *bcsH* open reading frame encodes a ~37-kDa protein (herein referred to as BcsH^{FL}) and, as shown in Fig. 3A, is preceded by a conserved ribosome binding site, or RBS, motif (*23*). The corresponding polypeptide sequence features an extremely high percentage of proline and other small neutral amino acids. Although such amino acid content suggests an intrinsically disordered tertiary structure (Fig. 3, B and C), proline-rich regions in general can play important roles in signaling and scaffolding proteins (*24*, *25*). An earlier study reported that recombinant expression constructs encoding full-length and N-terminally truncated BcsH-EGFP fusions, based on alternative open reading frames within the *bcsH* gene, invariably led to the expression of a fluorescently tagged ~8-kDa protein encompassing the C-terminal region of the annotated polypeptide chain (i.e., BcsH^{CTD}) (*20*). Moreover, functional complementation assays using plasmid-based expression of the BcsH^{CTD} variant in the *bcsH* knockout strain Cel-1 led to recovery of cellulosic pellicle formation (*20*). This further supports a model where, instead of being a relatively large disordered protein, the actual BcsH subunit is a short

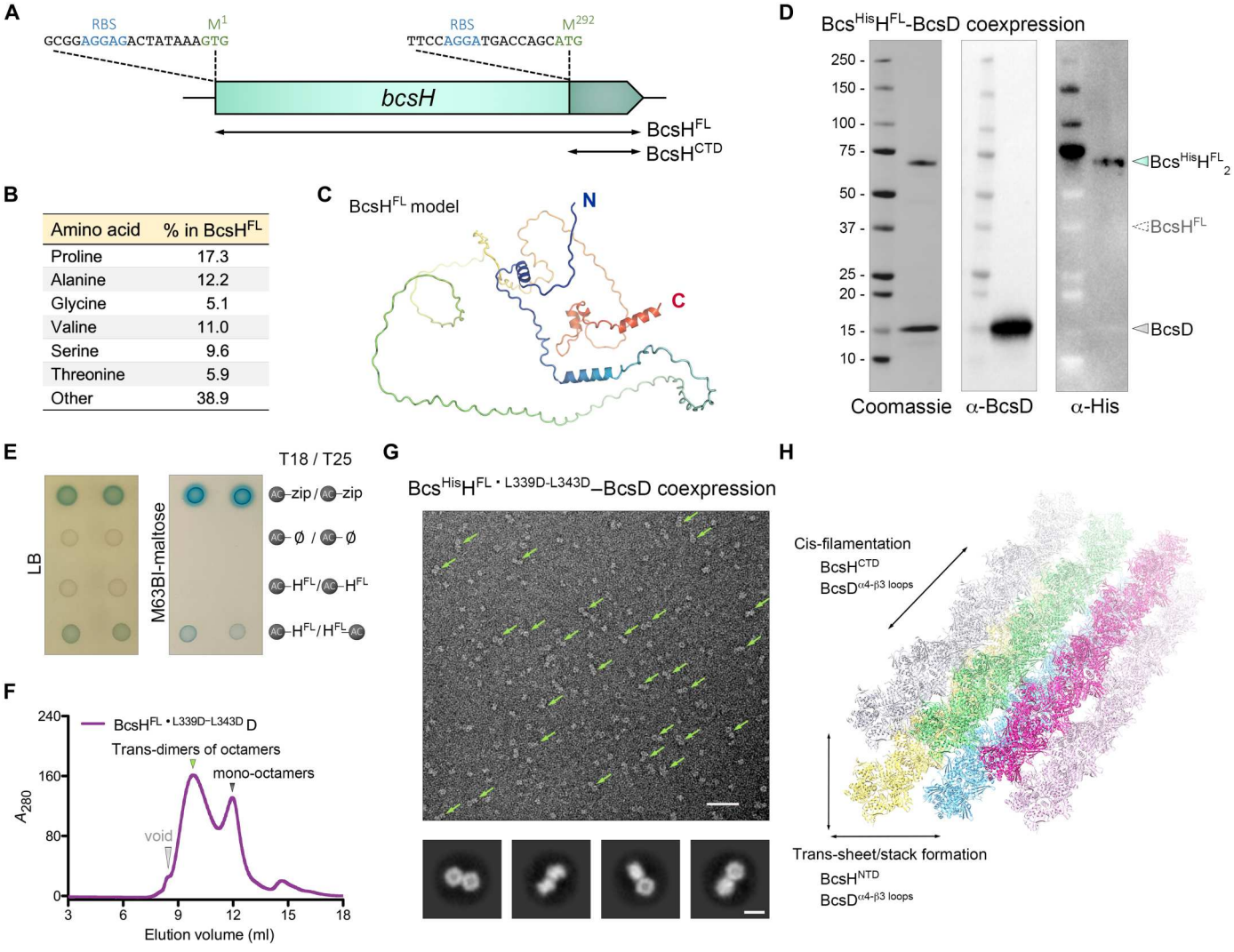

Fig. 3. Higher-order macromolecular assemblies. (**A**) Schematic representation of the BcsH open reading frame with putative ribosome binding and translation start sites. RBS, ribosome-binding site. (**B**) Amino acid content of full-length BcsH. (**C**) Fold prediction for full-length BcsH (AlphaFold2). (**D**) Coexpression and copurification of BcsH^{FL}–BcsD. Left: SDS-PAGE–migrated IMAC-eluted sample after purification through Bcs^{His}H^{FL}. Middle: Western blot detection of the eluted BcsD using an anti-BcsD antibody. Right: Western blot detection of the eluted Bcs^{His}H using an anti-His antibody. The theoretical molecular weights for a BcsH^{FL} monomer versus dimer are indicated. (**E**) Bacterial two-hybrid assay of interactions between BcsH^{FL} subunits based on split adenylate cyclase protein fusions and interaction-dependent functional reconstitution in a *cya*-deficient *E. coli* strain. The positive zip/zip control is based on coexpressed adenylate cyclase fragments each fused to a homodimerizing leucine zipper region of the yeast protein GCN4. Interactions were evaluated by the growth of blue colonies on supplemented LB or M63BI agar (see Materials and Methods). (**F**) Size-exclusion chromatography on a Superdex 200 Increase column for the purified BcsH$^{FL•L339D-L343D}$–BcsD complex. (**G**) Top: A representative negative-stain electron micrograph for the IMAC elution fraction of purified BcsH$^{FL•L339D-L343D}$–BcsD. Dimer-of-octamer species are highlighted with green arrows. Scale bar, 50 nm. Bottom: Representative views (2D class averages) with a scale bar of 10 nm. (**H**) Schematic representation of higher-order BcsHD polymers stabilized by BcsH-BcsH, BcsH-BcsD, and BcsD-BcsD interactions.

polypeptide able to tether BcsD to the linear TC nanoarray and thus determine crystalline cellulose secretion in vivo.

In agreement with these results, we were unable to purify stable, N-terminally tagged $BcsH^{FL}$ protein. Unexpectedly, however, when coexpressed with BcsD, $Bcs^{His}H^{FL}$ expressed as a stable, higher molecular weight protein, capable to copurify BcsD similarly to the $Bcs^{His}H^{CTD}$ construct. Moreover, SDS–polyacrylamide gel electrophoresis (SDS-PAGE) and Western blot analyses of the immobilized metal affinity chromatography (IMAC)–eluted $Bcs^{His}H^{FL}$-BcsD complex revealed that $BcsH^{FL}$ forms SDS- and heat-resistant dimeric species (Fig. 3D), likely due to the presence of the proline-rich N-terminal regions. In cellulo bacterial two-hybrid assays based on the functional complementation of split adenylate cyclase protein fusions (*26*) further corroborated specific, head-to-tail interactions between $BcsH^{FL}$ subunits (Fig. 3E). As the purified $Bcs^{His}H^{FL}$–BcsD complex yielded primarily large, electron-dense species not suitable for EM observation, we examined the effects of the C-terminal hydrophobic plug-disrupting $L^{339}D$-$L^{343}D$ double mutation in the full-length BcsH protein in vitro. As shown above, while the double BcsH mutant is still able to copurify BcsD through hydrophobic interactions within the intrasubunit BcsD pockets, it is completely incompetent to drive cis-filamentation of the copurified BcsD octamers (Fig. 2E).

In agreement with the above results, IMAC elution fractions of the purified $Bcs^{His}H^{FL\_L339D\text{-}L343D}$–BcsD complex revealed a mixture of monomeric and dimeric BcsD octamers, which eluted as two distinct peaks upon gel filtration (Fig. 3, F and G). As the mutant is unable to induce cis-filamentation, the observed dimeric species are likely driven by the head-to-tail interactions determined by the presence of the N-terminal BcsH regions. Together, these data support the formation of higher-order BcsHD polymers, likely driven by full-length BcsH-BcsH and BcsH-BcsD interactions and possibly stabilized by both cis- and trans-contacts between the α4-β3 loops of polymerized BcsD octamers (Fig. 3H).

In situ observation of BcsHD polymers and interactions with the synthase TCs

As discussed above, BcsD is an approximately 17-kDa protein that assembles into stable octamers with cylindrical architecture in which the protomers′ N termini localize in the internal lumen to separate it into four independent passageways (*7*), also visible in the herein presented cryo-EM data (Fig. 1D). On the basis of limited biochemical evidence (*19*), the protein has been proposed to partition primarily to the periplasm; however, its primary structure does not feature a detectable signal peptide (SP) for periplasmic export (Fig. 4A). Furthermore, plasmid-based expression of the annotated *bcsD* gene complemented cellulosic pellicle formation in a *bcsD*-disrupted strain, whereas N-terminally truncated variants missing the sixth (Lys^6) residue or beyond failed to overcome the cellulose secretion defect of the *bcsD* mutant in vivo (*7*). Together, these data exclude the role of an alternative translation start site for *bcsD* in the genome, as well as the presence of a cleavable SP in the expressed and folded multimeric protein. Similarly to BcsD, $BcsH^{FL}$ does not feature a detectable SP for sorting to the periplasm (Fig. 4A), and the functional complementation of cellulose secretion by plasmid-borne $bcsH^{CTD}$ in the Cel-1 genetic context (*20*) further rules out the role of a cryptic export signal at the N-terminal end of the protein.

Although BcsH is limited to the *Gluconacetobacter* lineage, BcsD homologs are encoded by many *bcs* operons of phylogenetically diverse bacterial species (*4*, *5*). To further examine possible sorting mechanisms for the two proteins, we reanalyzed all BcsD and BcsH homologs from their respective protein families, PF03500 and PF17040, as found in the Pfam protein database (table S1) (*27*). We used the recently reported SignalP 6.0 prediction tool, which is based on protein language models using information from millions of unannotated protein sequences across all domains of life and is able to reliably detect all five types of protein export signals, as well as functional subregions within the various SPs (*28*). Whereas prediction results for the rest of the Bcs components encoded by the *bcs1* operon were largely in line with the expected protein topologies and functions, not even one of the analyzed BcsH or BcsD homologs presented a detectable SP, of any sort (Fig. 4A and table S1).

We next used in cellulo cryo-EM imaging to visualize the morphology and localization of BcsHD filaments in both heterogeneous and native protein expression contexts (Fig. 4, B to E, and figs. S4 to S6). In line with the above analyses, the coexpression of $BcsH^{CTD}$ and BcsD in *E. coli* Star BL21 (DE3) led to the assembly of filaments with cytosolic, and not periplasmic, localization (Fig. 4, B to D, and fig. S4A). To corroborate this observation, we also constructed a recombinant BcsD-mCitrine fusion, which was found to be stable, capable to copurify with $BcsH^{CTD}$ and fluorescent, thus consistent with cytosolic protein localization (fig. S4B) (*29*–*31*).

Regardless of the small in situ cryo-EM dataset, the overall dimensions and morphology of the observed cytosolic filaments were consistent with those of the purified $BcsH^{CTD}$-BcsD beads-on-a-string polymers described above (Fig. 4, C and D). The $BcsH^{CTD}$–BcsD filaments were arranged in visible 3D stacks (Fig. 4, B to D). These are possibly stabilized by trans-interactions between the α4-β3 loops of polymerized BcsD octamers and/or macromolecular crowding effects in the cytosol (*32*), which can explain the sufficiency of $BcsH^{CTD}$ for functional complementation of the cellulose secretion defect in the Cel-1 genetic background (*20*).

As cytosolic localization of the BcsHD filaments might be due to interspecies export signal divergence, lack of endogenous binding partners, or overexpression effects overloading the *E. coli* protein sorting platforms, we next aimed to image the BcsHD filaments in their native context, namely, in biofilm-forming, crystalline cellulose–secreting *G. hansenii* cells in situ (Fig. 4E and fig. S5). As reported previously, the Bcs TCs in the bacterium arrange in a straight line along the longitudinal axis of the cell rod to allow for the exiting nascent polysaccharidic chains to arrange into the parallel microfibers of the so-called CR (fig. S5A) (*14*, *16*). The latter would then exit and grow from the cell pole and serve as a motility organelle, by propelling the cells in direction opposite to that of CR elongation; as a flotation device, by expulsing the cells to the air-liquid interface; and as a biofilm scaffold, by interweaving with other cells and their extracellular matrix components (*5*, *14*). We used cryo-EM to image the CR-underlying periplasmic space at high resolution; however, despite the observation of an electron-denser region underneath the outer membrane, we failed to identify macromolecular structures consistent with the formation of BcsHD filaments or higher-order lattice-like macromolecular assemblies (fig. S5B).

Our results are consistent with a recent cryo–electron tomography study that examined in detail the CR structure and underlying

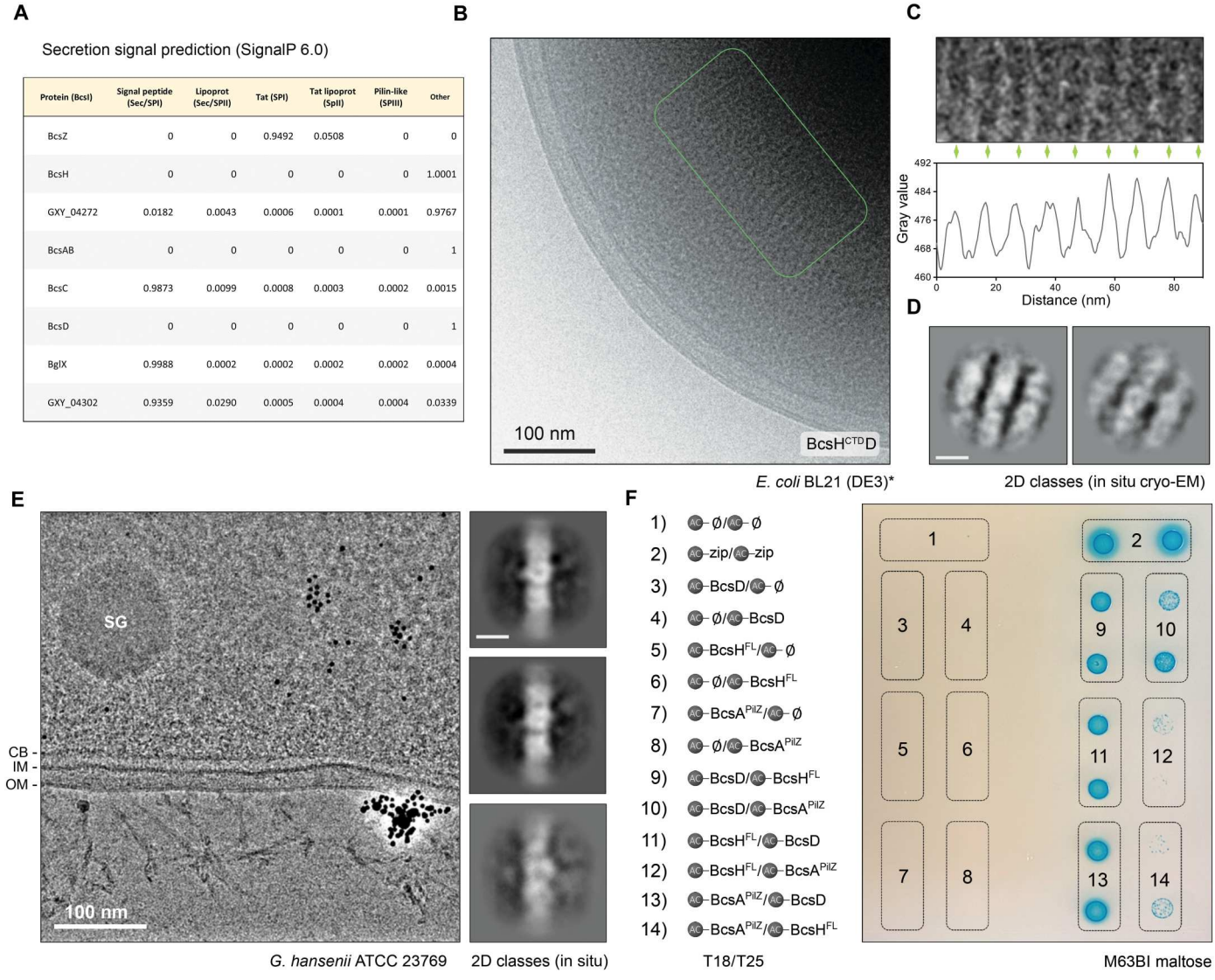

Protein (BcsI)	Signal peptide (Sec/SPI)	Lipoprot (Sec/SPII)	Tat (SPI)	Tat lipoprot (SpII)	Pilin-like (SPIII)	Other
BcsZ	0	0	0.9492	0.0508	0	0
BcsH	0	0	0	0	0	1.0001
GXY_04272	0.0182	0.0043	0.0006	0.0001	0.0001	0.9767
BcsAB	0	0	0	0	0	1
BcsC	0.9873	0.0099	0.0008	0.0003	0.0002	0.0015
BcsD	0	0	0	0	0	1
BglX	0.9988	0.0002	0.0002	0.0002	0.0002	0.0004
GXY_04302	0.9359	0.0290	0.0005	0.0004	0.0004	0.0339

Fig. 4. In situ BcsHD visualization and additional protein-protein interactions. (**A**) SP prediction in proteins encoded by the *bcs1* gene cluster, according to SignalP 6.0. (**B**) A representative cryo-EM micrograph of BcsH^{CTD}–BcsD coexpressing *E. coli* BL21 Star (DE3) cell. A low pass–filtered version of the micrograph, as well as additional snapshots, are presented in fig. S4. BcsH^{CTD}D filaments presenting a striated pattern are highlighted with a green box. (**C**) A zoomed-in region showing a stack of parallel filaments, with the corresponding gray intensity values plotted against distance in nanometers below. (**D**) In situ 2D class averages of the recombinantly expressed BcsHD filaments. Scale bar, 10 nm. (**E**) Left: A representative cryo-EM micrograph of a *G. hansenii* ATCC 23679 cell. SG, storage granule; CB, cortical belt; IM, inner membrane; OM, outer membrane. Secreted cellulose filaments are seen as bundles. Right: Representative 2D class averages of the cortical belt. Scale bar, 10 nm. (**F**) Bacterial two-hybrid assay of interactions between BcsD, BcsH^{FL}, and the BcsA^{PilZ} domain based on split adenylate cyclase protein fusions and interaction-dependent functional reconstitution in a *cya*-deficient *E. coli* strain. Positive zip/zip control as above. Interactions were evaluated by the growth of blue colonies on supplemented M63BI agar (see Materials and Methods).

cellular morphology of isolated and biofilm-embedded *Gluconacetobacter* cells (*14*). The same study also reported that the extracellular CR localization spatially correlates with a large intracellular structure—the cortical belt (fig. S5A)—that appeared specific for the *Gluconacetobacter* lineage of crystalline cellulose superproducers. The similarity of the cortical belt with cytoskeletal elements and its spatial correlation with the nascent CR led the authors to propose that it could be a cytoskeletal element organizing the membrane-embedded cellulose synthase complexes, similarly to the cortical microtubules in plants (*14*). Moreover, the tens of nanometers wide and hundreds of nanometers long structure was often found to present extensive regions of several stacked sheets underneath the inner membrane, with peak-to-peak spacing of approximately 15 ± 5 nm (*14*). As these characteristics are markedly similar to those of the heterogeneously expressed BcsHD filaments observed in situ (Fig. 4, B to D), we decided to image and analyze the so-called cortical belt at higher resolution. Despite the overall thickness of the *G. hansenii* cells and the surrounding vitreous ice, the representative side views of the cortical belt showed marked resemblances to the BcsHD polymers, including filament thickness, beads-on-a-string

polymerization pattern, and apparent size and morphology of the repeating units (Fig. 4E and fig. S5B). In addition, we screened extensively *bcsH*-deficient cells from the Cel-1 *G. hansenii* strain and were unable to find cortical belt–like structures in proximity to the cell membrane (fig. S6).

Although these results are in line with the absence of periplasmic export signals for both BcsD and BcsH, they are particularly unexpected considering a recent study that reports direct interactions of BcsD with the BcsAB synthase complex, as well as indirect interactions through cellulose with BcsC′s periplasmic modules (*33*). Furthermore, a transposon-based disruption of *bcsH* was previously reported to affect the stability of both BcsB and BcsC, but not BcsA (*34*), which has been largely interpreted as evidence for direct involvement of BcsH in periplasmic protein-protein interactions. Nevertheless, the latter study also showed that BcsA disruption itself is sufficient to induce similar, if not more pronounced, instability of the BcsB and BcsC components (*34*). Also, the presence of wild-type BcsA levels in the *bcsH* mutant suggests that the BcsA presence alone is not sufficient for BcsBC stabilization and raises the possibility that BcsH-driven synthase arrangement into linear TC arrays is what actually secures the proper assembly and stability of the secretion system. In addition, whereas BcsD-BcsAB interactions can be driven by either periplasmic or intracellular modules of the synthase complex, cellulose-dependent BcsD-BcsC interactions can be explained with independent interactions of the two proteins with glycosidic polymers, which is consistent with their so far reported functions (*5*). Last, whereas alternative export pathways for the two proteins can be envisioned—for example, twin-arginine translocase (TAT)-dependent export of the monomers via interactions with BcsZ as a chaperone—the relatively high copy numbers of BcsH and BcsD in the assembled filaments would require large amounts of chaperone partners and substantial energy expenses in an already costly biosynthetic process.

We therefore hypothesized that at least a significant part of the BcsH and BcsD subunits evade periplasmic export and instead determine crystalline cellulose secretion by participating in the assembly of an intracellular cytoskeleton—also known as the cortical belt—to secure an inside-out mechanism for TC nanoarray assembly. To test this orthogonally, we constructed split-adenylate cyclase protein fusions for functional bacterial two-hybrid complementation assays. We chose the regulatory $BcsA^{PilZ}$ domain as changes in its orientation relative to the catalytic glycosyl transferase domain are likely to accompany synthase activation (*5*), whereas its reported posttranslational detachment from the synthase polypeptide chain (*18*) and the presence of an amphipathic helical extension C-terminal to the PilZ β-barrel (*5*) can secure the conformational flexibility necessary to span the inner membrane–to–cortical belt distance (~24 nm) (*14*). We found that BcsD partakes in specific interactions with $BcsA^{PilZ}$ (Fig. 4F and fig. S7), further supporting an intracellular role for these key cellulose crystallinity determinants. Although $BcsH^{FL}$ is unstable in the absence of coexpressed BcsD, weak $BcsH^{FL}$-$BcsA^{PilZ}$ interaction signals were also detected in the bacterial two-hybrid experiments, suggesting additional synthase-stabilizing interactions. Last, expression of the recombinant BcsD-mCitrine fusion discussed above also exhibited characteristic fluorescence in cellulo, further supporting cytosolic localization (fig. S4C).

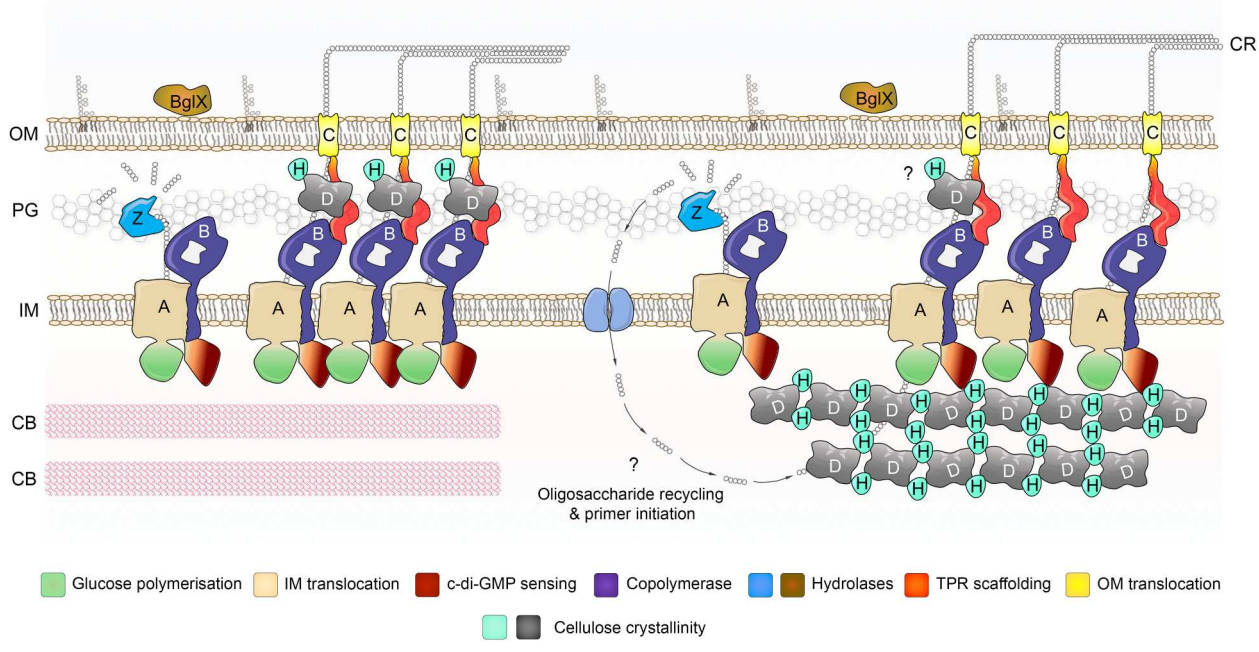

Fig. 5. A revised model for crystalline cellulose secretion. Thumbnail representations of the generally postulated model for Bcs subunit topology (left) versus a revised model integrating herein presented data on BcsHD structure, localization, and interactions. The proposed oligosaccharide uptake and recycling, as well as a putative role in the periplasm as previously proposed, remain to be further examined. A detailed review of the role of the additional Bcs subunits and their functionally important modules can be found in (*5*). OM, outer membrane; PG, peptidoglycan; IM-inner membrane; CB, cortical belt; CR, cellulose ribbon; TPR, tetratricopeptide repeats.

A revised model for crystalline cellulose secretion

Bacteria produce a remarkable diversity of physiologically, medically, and/or biotechnologically important secreted glycans, many of which are released by cooperative, multicomponent, synthase-dependent secretion nanomachines (*5*). Of these, the cellulose-extruding TCs of bacteria from the *Gluconacetobacter* lineage represent probably the longest-studied model system for synthase-dependent polysaccharide secretion and, hence, have provided the fundamentals of our current understanding of this important biosynthetic process. Despite decades-long scientific investment, however, many of the underlying molecular principles and regulatory inputs remain to be yet uncovered.

Important characteristics of the *Gluconacetobacter* cellulose are its purity, excellent water retention capacity, microporosity, transparency, tensile strength and elasticity, thermal and chemical stability, biodegradability, functionalization potential, and low antigenicity and implantability (*5*). These make the bacterial polymer a preferred material over plant-derived sources for a large variety of biotechnological applications, and the engineering of cost-effective approaches for industrial scale production is of continuous interest. Most of the above properties are directly related to the polysaccharide's high degree of crystallinity, which is itself strictly dependent on the formation of longitudinal TC nanoarrays with key, but so far enigmatic roles for the BcsD and BcsH accessory subunits. Here, we combined single-particle and in situ cryo-EM, in cellulo protein complex reconstitution and functional complementation, and in vitro biochemical assays to demonstrate that BcsH and BcsD form unique 3D macromolecular assemblies, likely involved in inside-out control of crystalline cellulose secretion (Fig. 5). Namely, we show that bridging hydrophobic interactions of the C-terminal region of BcsH with distinct BcsD octamers drives cis-filamentation into beads-on-a-string BcsHD polymers. We further show that, contrary to earlier reports, full-length BcsH can express as stable, SDS-resistant dimers and thus drive the formation of higher-order BcsHD assemblies, markedly similar to the recently reported "cortical belt" cytoskeletal element (*14*). Last, we provide protein interaction data that corroborate interactions of the crystallinity determinants with the synthases' regulatory PilZ modules and support an intracellular role for BcsHD in TC array formation (Fig. 5), not unlike the tethering of membrane-embedded cellulose synthase complexes by cortical microtubules in plants.

These findings raise at least one very important question, namely, what is the role of oligosaccharide binding in the luminal passageways of BcsD, which has been reported in cocrystallization experiments and has been proposed to prevent aggregative interactions between glucan chains in the periplasm (*5*, *7*). One possibility is that a subpopulation of expressed BcsH and BcsD are nevertheless exported in the periplasm to fulfill such a polysaccharide-shielding role during cellulose export. Whereas the herein presented data support cytosolic localization for the two proteins, multiple examples exist in the literature where known cytosolic proteins have been proposed to moonlight as extracytosolic actors with various specialized functions (*35*, *36*).

Alternatively, it is possible that the proteins participate in cytosolic substrate channeling rather than periplasmic product sorting (Fig. 5). The question of cellulose synthesis initiation remains open, and whereas some have proposed direct polymerization initiation onto a single glucose molecule, other studies have suggested that at least some bacterial and plant cellulose synthases can use oligosaccharidic primers to initiate catalysis (*5*). Multiple in vitro studies have shown, for example, that purified synthase complexes are catalytically active upon the simple addition of activating c-di-GMP, the substrate uridine diphosphate glucose (UDP-glucose), and divalent metal ions. Nevertheless, all high-resolution structures of cellulose synthases to date have shown the presence of a copurified translocating polysaccharide in the synthase export channel, therefore precluding the assumption of primerless initiation by similarly purified proteins in vitro (*5*). On the other hand, studies on *Agrobacterium tumefaciens* and *Gossypium hirsutum* (cotton) have suggested direct involvement of lipid-linked oligosaccharidic intermediates in cellulose biogenesis (*37*, *38*). It is also important to note that two of the *bcs1*-encoded enzymes, BcsZ and BglX, are actually hydrolases designed to degrade cellulosic polymers and yet are necessary for optimal cellulose secretion, presumably by minimizing abortive secretion, quality control of the secreted polysaccharide, or carving exogenous polymers found in the natural ecological niche of the bacterium (*5*). This means that, at any given time, there will be important amounts of released oligosaccharidic species in the periplasm or extracellular milieu. Given that bacteria are "omnivorous" and can import a variety of oligosaccharidic species for direct incorporation in their carbon metabolism (*39*), it is therefore possible that intracellular BcsHD can partake not only in TC array stabilization but also in oligosaccharide recycling for efficient cellulose strand initiation (Fig. 5).

We believe that the putative role of synthase-priming mechanisms and the full composition of the recently discovered cortical belt need to be further examined, by both in vitro biochemical and high-resolution, high-throughput in situ imaging studies. A better understanding of the cellulose crystallinity determinants can lead to the engineering of bacterial strains or tailored chemi-enzymatic systems for the production of optimized BC and also potentially yield tailored molecular scaffolds for increased efficiency and metabolic flux in other bacterial biosynthetic pathways. Approaches for the expression of Gluconacetobacter Bcs subunits, including BcsD and BcsH, in alternative species such as *E. coli* have already had some but limited success in inducing crystalline cellulose secretion recombinantly (*40*–*42*), and dissecting the underlying molecular mechanisms has the potential to greatly facilitate such bioengineering efforts. Similarly, c-di-GMP–dependent synthase activation through the enzymes' PilZ domains should be examined in the bigger picture of synthase–cortical belt interactions. Together, this study provides the first high-resolution insights into the formation of 3D Bcs scaffolds and crystalline cellulose secretion by the economically relevant superproducer *G. hansenii* and lays the foundation for more comprehensive pan-envelope models of TC nanoarray assembly and regulation.

MATERIALS AND METHODS

The experiments were not randomized, and the investigators were not blinded during experimental design, execution, or outcome assessment. Nevertheless, many of the experiments were reproduced independently by different investigators, including EM and biochemical and phenotypic assays.

Bacterial strains

Plasmids for recombinant protein expression (see below) were propagated in and isolated from *E. coli* DH5α cells using Lennox LB and LB agar medium supplemented, as applicable, with the following concentrations of antibiotics: ampicillin (100 μg/ml; for pET21b, pProEx-Htb, and pUT18C variants), kanamycin [40 μg/ml; for pRSFDuet1* and pK(N)T25 variants], and chloramphenicol (34 μg/ml; for pSEVA331Bb variants). All recombinant protein expression for structural and in vitro biochemical studies was carried out in *E. coli* BL21 Star (DE3) cells using LB agar and liquid TB (terrific broth) medium, supplemented with the appropriate antibiotics [ampicillin (100 μg/ml) for pProEx-Htb–based expression and a combination of ampicillin (70 μg/ml) and kanamycin (30 μg/ml) for pRSFDuet1* and pProEx-Htb–based coexpression]. Functional complementation assays were carried out in the *Gluconacetobacter* Cel-1 strain using *bcsH* variants cloned into the pSEVA331Bb plasmid modified to carry promoter J23104 for constitutive recombinant protein expression (*20*, *22*, *43*). An empty pSEVA331Bb vector and the wild-type *G. hansenii* ATCC23769 were also used in control experiments. pSEVA331Bb-PJ23104–driven expression was additionally used for the expression of a recombinant BcsD-mCitrine fusion in *Gluconacetobacter* cells. All *Gluconacetobacter* cultures were grown in SH (Schramm and Hestrin) (*44*) (2% glucose, 0.5% bactopeptone, and 0.5% yeast extract at pH 6.0) or SH agar medium supplemented with chloramphenicol (340 μg/ml), where applicable. Last, bacterial two-hybrid experiments were performed using supplemented LB and M63BI agar plates, chemically competent bEYY2122 (BTH101 Δ*cyaA*) cells, and the isopropyl-β-D-thiogalactopyranoside (IPTG)–inducible pKT(N)25 and pUT18C expression plasmids with custom-modified multiple cloning sites (MCS; see below) (*45*, *46*).

Recombinant DNA techniques

DNA manipulations were carried out using the standard protocols for polymerase chain reaction (PCR), molecular cloning, transformation, and DNA analysis. Coding regions for BcsD, $BcsH^{FL}$, $BcsH^{CTD}$, and $BcsA^{PilZ}$ were amplified using high-fidelity Phusion DNA polymerase (New England Biolabs) and *G. hansenii* genomic DNA as a template and inserted via digestion/ligation cloning into IPTG-inducible expression vectors with custom-modified MCS. Point mutations and MCS modifications were performed using inverse PCR-based protocols and mutation-specific oligonucleotides as primers (table S2). Expression vectors for plasmid-based expression of *bcsH* and *bcsD* variants in *G. hansenii* Cel-1 cells (see below and table S2) were constructed by overlap extension PCR and blunt-end ligation. All recombinant vectors and introduced mutations were verified by DNA sequencing and, where applicable, IPTG-inducible protein expression.

Protein expression and purification

The coding regions corresponding to BcsD, $BcsH^{FL}$ (M^{1}-SASGS...NEEES^{353}), and $BcsH^{CTD}$ (M^{292}TKTDT...NEEES^{353}) were PCR-amplified and introduced into a modified pProEx-Htb expression vector to yield IPTG-inducible variants carrying N-terminal hexahistidine tags cleavable by the human rhinovirus (HRV) 3c protease ($Bcs^{His}D$, $Bcs^{His}H^{FL}$, and $Bcs^{His}H^{CTD}$). In parallel, a pRSF-Duet1 vector was PCR-amplified with primers CATATGGGATCCCATGGTATATCTCCTTATTAAAG and CTCGAGGCGGCCGCATAATGCTTAAGTCGAACAGA to remove the hexahistidine tag coding region and used in BamHI/NotI restrictase–mediated cloning to insert the DNA sequence corresponding to full-length untagged BcsD for coexpression with pProEX-Htb–encoded BcsH variants. Last, a synthetic BcsD-GSAGGSG-mCitrine fusion was cloned by overlap extension PCR into pRSFDuet1* for similar coexpression experiments (restrictase-based cloning) or into pSEVA331Bb for expression in *G. hansenii* (overlap extension PCR-based cloning).

For recombinant protein expression, all expression vectors were freshly (co)transformed into chemically competent *E. coli* BL21 Star (DE3) cells and plated onto antibiotics-supplemented LB agar plates [ampicillin (100 μg/ml) or a combination of ampicillin (70 μg/ml) + kanamycin (30 μg/ml) for coexpressed vectors]. Resultant colonies were then inoculated and grown aerobically at 37°C in TB medium supplemented with the appropriate antibiotics. At a cell optical density corresponding to an optical density of 0.8 to 1.0 at 600 nm (OD_{600}), the cells were moved to 17°C and overnight protein expression was induced by the addition of IPTG at a final concentration of 0.7 mM. After 16 hours, cells were harvested by centrifugation (20 min at 4000*g* and 4°C), resuspended in lysis buffer [20 mM Hepes (pH 8.0), 100 mM NaCl, 18 mM imidazole (pH 8.0), and 1 tablet/50 ml of c*O*mplete protease inhibitors (Roche)], and flash-frozen in liquid nitrogen. For protein purification, cells were thawed and lysed by sonication. Cell debris were removed by centrifugation (1 hour at 30,000*g* and 4°C), and the cleared lysates were loaded onto buffer-washed TALON Superflow resin (GE Healthcare) at approximately 0.5 to 1 ml of resin per liter of culture. The resin was subsequently washed with more than 20 volumes of IMAC buffer A (protease inhibitor–free lysis buffer as above), and bound proteins were eluted in a single step with IMAC buffer B [IMAC buffer A supplemented with 200 mM imidazole (pH 8.0)]. The eluted proteins ($Bcs^{His}D$) and protein complexes (wild-type and mutant $Bcs^{His}H^{FL}$-BcsD and $Bcs^{His}H^{CTD}$-BcsD) were subsequently concentrated to 2.5 ml using an Amicon Ultra centrifugal filter (50-kDa cutoff; Millipore) and desalted using disposable PD-10 desalting columns (GE Healthcare) and desalting buffer [20 mM Hepes (pH 8.0), 100 mM NaCl, and 12 mM imidazole]. The protein fractions were then incubated at 4°C overnight with His-tagged HRV3c protease for removal of the hexahistidine tags from the recombinant Bcs constructs. Cleaved proteins and copurified partners were collected in the flow-through fraction during reverse IMAC chromatography on the following day and after concentration were subjected to size exclusion chromatography on a Superdex 200 Increase 10/300 GL column equilibrated with gel filtration buffer [20 mM Hepes (pH 8.0) and 100 mM NaCl]. Collected protein fractions were analyzed for purity, concentrated, and used for cryo-EM grid preparation, where applicable, at concentrations of approximately 0.5 mg/ml ($BcsH^{CTD}D$) to 1.8 mg/ml (BcsD) using glow-discharged Quantifoil R1.2/1.3 gold grids and a Vitrobot Mark IV device (Thermo Fisher Scientific) (4°C, 100% humidity, plunge-freezing in liquid ethane). Excess proteins were aliquoted and flash-frozen for storage at −80°C.

SDS-PAGE and Western blot analyses

Protein fractions were analyzed by the standard denaturing SDS-PAGE electrophoresis using 4 to 20% gradient mini-gels (Bio-Rad), Expedeon InstantBlue Coomassie stain, and a Gel Doc EZ system (Bio-Rad) for Coomassie stain visualization. For Western blot analyses, SDS-PAGE migrated proteins were directly

transferred using a standard mini-gel transfer protocol, polyvinylidene difluoride (PVDF) membranes, and a Trans-blot Turbo transfer system (Bio-Rad). Blocking and antibody incubations were done in the presence of 5% skim milk in 0.1% Tween 20 in 1x phosphate buffered saline (TPBS), and all washes between and after antibody incubations were done with 1× TPBS buffer. Goat horseradish peroxidase (HRP)–conjugated anti-His_6 (dilution 1:1000; Abcam, ab1269) and newly raised rabbit anti-BcsD (dilution 1:2000; available upon request) antibodies were used as primary; HRP-conjugated anti-rabbit antibody (dilution 1:6000; GE Healthcare Bio-Sciences, NIF824) was used as secondary. Signals were visualized using the Clarity Western ECL substrate and a ChemiDoc imaging system (Bio-Rad).

Negative-stain EM

Negative-stain single-particle EM was used for direct visualization of the IMAC elution fraction of a purified $Bcs^{His}H^{FL}$ variant carrying the cis-filamentation–disruptive $L^{339}D$-$L^{343}D$ double mutation upon coexpression with BcsD ($Bcs^{His}H^{FL\_L339D\text{-}L343D}$–BcsD). Briefly, 5 μl of IMAC-eluted sample (concentrations, ~0.01 to 0.02 mg/ml) was spotted on glow-discharged carbon-coated copper grids (Agar Scientific). After 60-second incubation, the extra liquid was blotted off, and the grids were passed sequentially through three drops of 2% (w/v) uranyl acetate solution, with 30-second incubation in the last drop before blotting and air drying. Micrographs were taken on a Thermo Fisher Scientific FEI Tecnai F20 electron microscope operated at an accelerating voltage of 200 kV and equipped with a field emission gun and an Eagle 4k × 4k charge-coupled device (CCD) camera. Micrographs were collected with a nominal defocus range of −1.5 to −3 μm and a low dose of ~30 electrons/Å at a pixel size of 1.835 $Å^2$. Micrograph contrast transfer function (CTF) correction was performed with Gctf (*47*) through the cryoSPARC v3 interface (*48*), and autopicking and class averaging were performed with cryoSPARC's "Blob picker" and 2D classification tools, respectively.

Cryo-EM and single-particle analysis

To determine the structure of BcsD in solution, we collected a control dataset of 2419 movies on the Elsa Talos Arctica transmission electron microscope (Thermo Fisher Scientific) at the European Institute of Chemistry and Biology (IECB) Bordeaux operated at 200 kV and equipped with a Gatan K2 Summit direct electron detector. Movies of 46 frames were recorded using SerialEM in electron counting mode at a total exposure dose of 50.15 $e^-/Å^2$ and a corrected pixel size of 0.93 $Å^2$. The movies were motion- and CTF-corrected using MotionCor2 (*49*) and Gctf, respectively, after which all micrograph processing was continued in cryoSPARC v3. Particles were autopicked using the software's "Blob picker" function and, after 2D classification, class averages showing resolved secondary structure features were used as templates for a new round of template-based autopicking and 2D classification for best particle selection. Ab initio modeling with two classes yielded a single model consistent with the previously reported crystal structures of octameric BcsD, corresponding to 380,318 particles or roughly 84% of the preselected particles. Nonuniform (NU) refinements yielded final models at resolutions of 3.6 and 3.3 Å, using C1 and D4 symmetries, respectively. The higher-resolution electron density map was then used for iterative rounds of atomic model building in Coot (*50*) and refinement in Phenix (*51*) and Namdinator (*52*).

To determine the structure of BcsHD cis-filaments in solution, a dataset of 9163 movies with a total dose of 49.88 $e^-/Å^2$ was collected at the CM01 Titan Krios at the European Synchrotron Radiation Facility (ESRF), Grenoble (*53*), equipped with a Gatan K3 direct electron detector and a Gatan GIF Quantum LS energy filter. Following motion and CTF correction with MotionCor2 and Gctf, respectively, 6342 movies with CTF fit resolutions better than 4 Å and defocus in the 0.3- to 2.5-μm range were selected for downstream processing in cryoSPARC v3. Initial manual picking of about 3000 particles and 2D classification were used to generate templates for autopicking and extraction of 2,849,271 particles. Following two rounds of 2D classification and removal of noisy class averages, a total of 1,864,195 particles were selected for ab initio modeling and 3D classification using three 3D classes. A single model corresponding to 1,425,195 particles or roughly 76% of the preselected ones was consistent with beads-on-a-string polymerization of BcsD octamers. NU refinement yielded a refined 3D model at an average gold standard resolution of 2.7 Å. Following $BcsH^{CTD}D$ model building and refinement in Coot, Phenix, and Namdinator, the central two BcsD octamers and contacting BcsH fragments were further used for mask generation, particle subtraction, and local refinement, yielding a final NU-refined model at 2.6-Å resolution. In addition, the ensemble of particles were reextracted with a larger, slightly downsampled box and refined to 2.8-Å resolution for reliable rigid-body fitting of four adjacent BcsD octamers and connecting BcsH peptides. Coordinate refinement statistics are summarized in table S3, and the EM data processing strategies are shown in figs. S8 and S9.

In situ cryo-EM imaging

For in situ imaging of $BcsH^{CTD}D$ filaments heterogeneously expressed in *E. coli* BL21 Star (DE3), cells were collected following IPTG induction and overnight expression at 17°C, and washed with and resuspended in phosphate-buffered saline. Five microliters of the cell suspension was deposited on glow-discharged gold Quantifoil R3.5/1 grids (Quantifoil Micro Tools GmbH), and after 5 to 10 s, the grids were back-blotted with a Parafilm/Whatman paper sandwich and plunge-frozen in liquid ethane using a Vitrobot Mark IV device (Thermo Fisher Scientific) (20°C, 100% humidity). Movies were collected at the Elsa Talos Arctica (Thermo Fisher Scientific) microscope at the IECB, equipped with a 200 kV field emission gun and a Gatan K2 Summit direct electron detector (nominal magnification of 36,000×, pixel size of 1.18 $Å^2$, and total electron dose of 50 $e^-/Å^2$). Motion and CTF correction were performed with MotionCor2 and Gctf, respectively, and manual picking of about 450 particles and 2D classification were performed in cryoSPARC v3.

For in situ imaging of the cortical belt in isolated *G. hansenii* ATCC 23769 cells, bacteria were cultured under static conditions at 25°C in SH medium for cellulosic pellicle formation. Cells were then separated from the mature biofilm by mechanical agitation of the pellicle, pelleted by centrifugation (20°C, 10 min, 2500*g*), and resuspended in 0.5 ml of fresh SH medium. The mini-cultures were then incubated for 3 to 5 hours at 30°C, upon which gold Quantifoil R3.5/1 grids (Quantifoil Micro Tools GmbH) were glow-discharged. Four microliters of the cell suspension was mixed with 1 μl of bovine serum albumin–pretreated 10-nm colloidal gold nanoparticles in solution (Sigma-Aldrich) and then was deposited on each grid for 5 to 10 s before back-blotting and plunge-

freezing as above. Tilt series of six-frame movies were collected in electron counting with dose fractionation mode on the IECB Elsa Talos Arctica at a nominal magnification of 22,000×, a pixel size of 1.9 Å^2, 18 e$^-$/Å^2 per tilt, and a limited range of ±10° with 2° increments due to the relative thickness of the cells and the narrow architecture of the cortical belt. A separate set of tomograms were collected with a range of ±60° for cortical belt visualization. Following motion in MotionCor2, 472 micrographs with visible cortical belt structures were further processed in cryoSPARC v3. CTF correction was performed with the software's Patch CTF function, and cortical belt particles were manually picked, Patch CTF–extracted with box size of 220 pixels, and subjected to 2D classification.

In cellulo functional complementation assays

Bacterial two-hybrid assay

To probe protein-protein interactions in cellulo, we resorted to the bacterial split adenylate cyclase two-hybrid complementation assay (*26*). By PCR amplification, we first custom-modified the standard expression vectors pKT25, pKNT25, and pUT18C as described previously (*12*), to introduce BamHI and KpnI cloning sites in the respective MCS, while optimizing the number and type of exogenous amino acids to be added to the recombinant hybrids (table S2). Coding regions for full-length BcsD, BcsH (after removal of the intrinsic BamHI site), and BcsA^{PilZ} (BcsAB1$^{567–684}$) domains were then PCR-amplified with primers carrying the corresponding restriction sites, digested, and ligated into the modified vectors. All recombinant constructs were amplified in DH5α cells and verified by DNA sequencing. The bacterial two-hybrid assay was performed using standard protocols and the *E. coli* bEYY2122 strain [BTH101 Δ*cyaA* (*45*)]. Briefly, chemically competent *E. coli* bEYY2122 cells were cotransformed with derivatives of the pUT18C and pK(N)T25 vectors and plated on LB Miller agar supplemented with ampicillin (70 μg/ml) and kanamycin (30 μg/ml). Individual cotransformant colonies were picked and grown overnight at 37°C in liquid antibiotics-supplemented LB medium. The next morning, 4 μl of saturated culture was spotted onto LB Miller agar [supplemented with ampicillin (70 μg/ml), kanamycin (30 μg/ml), IPTG (0.1 mM), and 5-bromo-4-chloro-3-indolyl-beta-D-galacto-pyranoside (X-gal; 40 μg/ml)] or M63BI agar [supplemented with ampicillin (50 μg/ml), kanamycin (25 μg/ml), 0.1 mM IPTG, X-gal (40 μg/ml), and 0.2% maltose] plates. Protein interactions were evaluated after 24- to 30-hour incubation at 30°C by blue colony color in the case of LB Miller agar plates and by both colony growth and blue color in the case of M63BI agar plates. pUT18C and pKT25 vectors carrying the corresponding adenylate cyclase fragments but no recombinant fusions were used in cotransformations as negative controls, whereas cotransformants expressing pKT25-zip and pUT18C-zip vectors were used as positive controls. The latter vectors are derivatives of the pKT25 and pUT18C vectors in which the leucine zipper of Gcn4 (amino acid sequence: ... I Q R M K Q L E D K V E E L L S K N Y H L E N E V A R L K K L V G E R) is genetically fused in frame to the T25 and T18 adenylate fragments, respectively. The results are representative of at least three independent experiments and more than six biological replicates.

Cellulosic pellicle formation

For functional complementation assays in *G. hansenii*, we adapted previously reported protocols for culture growth and transformation (*43*). Wild-type and Cel-1 *G. hansenii* cultures were grown from single colonies at 30°C and under agitation in liquid SH medium supplemented with an enzyme blend of cellulases (1:1000 working concentration; SAE0020, Sigma-Aldrich). At mid-log phase (OD_{600} ~ 0.4 to 0.6), the cells were pelleted by centrifugation (14 min, 3200*g*, 4°C), washed two times with ice-cold 1 mM Hepes (pH 7.0) in water, and resuspended in ice-cold 15% glycerol in water. Plasmid DNA (3 to 5 μl) was added to 75 μl of the thus prepared electrocompetent cells and transferred to a pre-chilled 1-mm electroporation cuvette (Eurogentec). Electroporation was carried out using the Gene Pulser Xcell Total System (Bio-Rad) with a 10.2-ms exponential decay pulse of 2.4 kV, with 400-ohm resistance and 25-μF capacitance. The pulsed cells were then gently transferred into 800 μl of SH medium without antibiotics and grown under agitation at 30°C overnight. Following the overnight recovery, the cells were pelleted by centrifugation at 25°C, gently resuspended in a small volume of SH medium, and spread onto SH agar plates supplemented with chloramphenicol (340 μg/ml).

Single colonies of wild-type ATCC 23769 cells, the Cel-1 mutant, and Cel-1 cells complemented with empty pSEVA331Bb, pSEVA331Bb-PJ23104–*bcsH*^{FL}, or pSEVA331Bb-PJ23104–*bcsH*$^{FL\_L339D-L343D}$ were grown under agitation to mid-log phase in liquid SH medium supplemented with chloramphenicol (340 μg/ml), where applicable. Each culture was then diluted 100× in fresh medium and grown at 25°C in static conditions. Pellicle formation and *bcsH* functional complementation were qualitatively assessed by the ability of the cultured cells to float to the air-liquid interface and form a continuous cellulosic pellicle resistant to mechanical manipulation.

Additional bioinformatic tools

Protein sequences were analyzed using the National Center for Biotechnology Information (NCBI) BlastP suite (*54*), the Pfam database (*27*), and the Phyre2 (*55*), Robetta (*56*, *57*), and AlphaFold2 (*58*) fold prediction servers. Sequence alignments were done with Clustal Omega (*59*) and Jalview (*60*), and structural analyses were carried out using the DaliLite (*61*), PISA (*62*), 3V channel finder (*63*), and PDBsum (*64*) servers. Structure visualization was done in PyMOL (Schrödinger), Chimera (*65*), and ChimeraX (*66*).

Supplementary Materials

This PDF file includes:

Figs. S1 to S9
Tables S1 to S3

View/request a protocol for this paper from *Bio-protocol*.

REFERENCES AND NOTES

1. P. Ross, H. Weinhouse, Y. Aloni, D. Michaeli, P. Weinberger-Ohana, R. Mayer, S. Braun, E. de Vroom, G. A. van der Marel, J. H. van Boom, M. Benziman, Regulation of cellulose synthesis in *Acetobacter xylinum* by cyclic diguanylic acid. *Nature* **325**, 279–281 (1987).
2. U. Jenal, A. Reinders, C. Lori, Cyclic di-GMP: Second messenger extraordinaire. *Nat. Rev. Microbiol.* **15**, 271–284 (2017).
3. P. V. Krasteva, H. Sondermann, Versatile modes of cellular regulation via cyclic dinucleotides. *Nat. Chem. Biol.* **13**, 350–359 (2017).
4. U. Römling, M. Y. Galperin, Bacterial cellulose biosynthesis: Diversity of operons, subunits, products, and functions. *Trends Microbiol.* **23**, 545–557 (2015).
5. W. Abidi, L. Torres-Sánchez, A. Siroy, P. V. Krasteva, Weaving of bacterial cellulose by the Bcs secretion systems. *FEMS Microbiol. Rev.* **46**, fuab051 (2022).

6. J. T. McNamara, J. L. Morgan, J. A. Zimmer, A Molecular description of cellulose biosynthesis. *Annu. Rev. Biochem.* **84**, 895–921 (2015).
7. S. Q. Hu, Y. G. Gao, K. Tajima, N. Sunagawa, Y. Zhou, S. Kawano, T. Fujiwara, T. Yoda, D. Shimura, Y. Satoh, M. Munekata, I. Tanaka, M. Yao, Structure of bacterial cellulose synthase subunit D octamer with four inner passageways. *Proc. Natl. Acad. Sci. U.S.A.* **107**, 17957–17961 (2010).
8. J. F. Acheson, Z. S. Derewenda, J. Zimmer, Architecture of the cellulose synthase outer membrane channel and its association with the periplasmic TPR domain. *Structure* **27**, 1855–1861.e3 (2019).
9. L. Sun, P. Vella, R. Schnell, A. Polyakova, G. Bourenkov, F. Li, A. Cimdins, T. R. Schneider, Y. Lindqvist, M. Y. Galperin, G. Schneider, U. Römling, Structural and functional characterization of the BcsG subunit of the cellulose synthase in *Salmonella typhimurium*. *J. Mol. Biol.* **430**, 3170–3189 (2018).
10. A. J. Spiers, J. Bohannon, S. M. Gehrig, P. B. Rainey, Biofilm formation at the air-liquid interface by the *Pseudomonas fluorescens* SBW25 wrinkly spreader requires an acetylated form of cellulose. *Mol. Microbiol.* **50**, 15–27 (2003).
11. W. Thongsomboon, D. O. Serra, A. Possling, C. Hadjineophytou, R. Hengge, L. Cegelski, Phosphoethanolamine cellulose: A naturally produced chemically modified cellulose. *Science* **359**, 334–338 (2018).
12. W. Abidi, S. Zouhir, M. Caleechurn, S. Roche, P. V. Krasteva, Architecture and regulation of an enterobacterial cellulose secretion system. *Sci. Adv.* **7**, eabd8049 (2021).
13. A. M. Richter, A. Possling, N. Malysheva, K. P. Yousef, S. Herbst, M. von Kleist, R. Hengge, Local c-di-GMP signaling in the control of synthesis of the *E. coli* biofilm exopolysaccharide pEtN-cellulose. *J. Mol. Biol.* **432**, 4576–4595 (2020).
14. W. J. Nicolas, D. Ghosal, E. I. Tocheva, E. M. Meyerowitz, G. J. Jensen, Structure of the bacterial cellulose ribbon and its assembly-guiding cytoskeleton by electron cryotomography. *J. Bacteriol.* **203**, e00371-20 (2021).
15. P. Purushotham, R. Ho, J. Zimmer, Architecture of a catalytically active homotrimeric plant cellulose synthase complex. *Science* **369**, 1089–1094 (2020).
16. R. M. Brown, J. H. Willison, C. L. Richardson, Cellulose biosynthesis in *Acetobacter xylinum*: Visualization of the site of synthesis and direct measurement of the in vivo process. *Proc. Natl. Acad. Sci. U.S.A.* **73**, 4565–4569 (1976).
17. M. Bimmer, M. Mientus, A. Klingl, A. Ehrenreich, W. Liebl, The roles of the various cellulose biosynthesis operons in Komagataeibacter hansenii ATCC 23769. *Appl. Environ. Microbiol.* **88**, e0246021 (2022).
18. P. R. Iyer, Y. A. Liu, Y. Deng, J. B. McManus, T. H. Kao, M. Tien, Processing of cellulose synthase (AcsAB) from *Gluconacetobacter hansenii* 23769. *Arch. Biochem. Biophys.* **529**, 92–98 (2013).
19. P. R. Iyer, J. Catchmark, N. R. Brown, M. Tien, Biochemical localization of a protein involved in synthesis of *Gluconacetobacter hansenii* cellulose. *Cellul.* **18**, 739–747 (2011).
20. N. Sunagawa, T. Fujiwara, T. Yoda, S. Kawano, Y. Satoh, M. Yao, K. Tajima, T. Dairi, Cellulose complementing factor (Ccp) is a new member of the cellulose synthase complex (terminal complex) in *Acetobacter xylinum*. *J. Biosci. Bioeng.* **115**, 607–612 (2013).
21. C. E. Jahn, D. A. Selimi, J. D. Barak, A. O. Charkowski, The Dickeya dadantii biofilm matrix consists of cellulose nanofibres, and is an emergent property dependent upon the type III secretion system and the cellulose synthesis operon. *Microbiology* **157**, 2733–2744 (2011).
22. R. Standal, T. G. Iversen, D. H. Coucheron, E. Fjaervik, J. M. Blatny, S. Valla, A new gene required for cellulose production and a gene encoding cellulolytic activity in *Acetobacter xylinum* are colocalized with the bcs operon. *J. Bacteriol.* **176**, 665–672 (1994).
23. P. R. Iyer, S. M. Geib, J. Catchmark, T. H. Kao, M. Tien, Genome sequence of a cellulose-producing bacterium, *Gluconacetobacter hansenii* ATCC 23769. *J. Bacteriol.* **192**, 4256–4257 (2010).
24. M. P. Williamson, The structure and function of proline-rich regions in proteins. *Biochem. J.* **297**, 249–260 (1994).
25. J. Kühn, A. Briegel, E. Mörschel, J. Kahnt, K. Leser, S. Wick, G. J. Jensen, M. Thanbichler, Bactofilins, a ubiquitous class of cytoskeletal proteins mediating polar localization of a cell wall synthase in *Caulobacter crescentus*. *EMBO J.* **29**, 327–339 (2010).
26. G. Karimova, J. Pidoux, A. Ullmann, D. Ladant, A bacterial two-hybrid system based on a reconstituted signal transduction pathway. *Proc. Natl. Acad. Sci. U.S.A.* **95**, 5752–5756 (1998).
27. J. Mistry, S. Chuguransky, L. Williams, M. Qureshi, G. A. Salazar, E. L. L. Sonnhammer, S. C. E. Tosatto, L. Paladin, S. Raj, L. J. Richardson, R. D. Finn, A. Bateman, Pfam: The protein families database in 2021. *Nucleic Acids Res.* **49**, D412–D419 (2021).
28. F. Teufel, J. J. Almagro Armenteros, A. R. Johansen, M. H. Gíslason, S. I. Pihl, K. D. Tsirigos, O. Winther, S. Brunak, G. von Heijne, H. Nielsen, SignalP 6.0 predicts all five types of signal peptides using protein language models. *Nat. Biotechnol.* **40**, 1023–1025 (2022).
29. E. J. Banks, M. Valdivia-Delgado, J. Biboy, A. Wilson, I. T. Cadby, W. Vollmer, C. Lambert, A. L. Lovering, R. E. Sockett, Asymmetric peptidoglycan editing generates cell curvature in *Bdellovibrio* predatory bacteria. *Nat. Commun.* **13**, 1509 (2022).
30. A. Fay, N. Czudnochowski, J. M. Rock, J. R. Johnson, N. J. Krogan, O. Rosenberg, M. S. Glickman, Two accessory proteins govern MmpL3 mycolic acid transport in mycobacteria. *MBio* **10**, e00850-19 (2019).
31. B. J. Feilmeier, G. Iseminger, D. Schroeder, H. Webber, G. J. Phillips, Green fluorescent protein functions as a reporter for protein localization in *Escherichia coli*. *J. Bacteriol.* **182**, 4068–4076 (2000).
32. R. J. Ellis, Macromolecular crowding: Obvious but underappreciated. *Trends Biochem. Sci.* **26**, 597–604 (2001).
33. T. Kondo, Y. Nakamura, S. Nojima, M. Yao, T. Imai, The BcsD subunit of type I bacterial cellulose synthase interacts dynamically with the BcsAB catalytic core complex. *FEBS Lett.* (2022). 10.1002/1873-3468.14495.
34. Y. Deng, N. Nagachar, C. Xiao, M. Tien, T. H. Kao, Identification and characterization of non-cellulose-producing mutants of *Gluconacetobacter hansenii* generated by Tn5 transposon mutagenesis. *J. Bacteriol.* **195**, 5072–5083 (2013).
35. B. P. Girinathan, S. E. Braun, R. Govind, *Clostridium difficile* glutamate dehydrogenase is a secreted enzyme that confers resistance to H2O2. *Microbiology (Reading).* **160**, 47–55 (2014).
36. B. Jagadeesan, O. K. Koo, K. P. Kim, K. M. Burkholder, K. K. Mishra, A. Aroonnual, A. K. Bhunia, LAP, an alcohol acetaldehyde dehydrogenase enzyme in *Listeria,* promotes bacterial adhesion to enterocyte-like Caco-2 cells only in pathogenic species. *Microbiology* **156**, 2782–2795 (2010).
37. A. G. Matthysse, S. White, R. Lightfoot, Genes required for cellulose synthesis in A*grobacterium tumefaciens*. *J. Bacteriol.* **177**, 1069–1075 (1995).
38. L. Peng, Y. Kawagoe, P. Hogan, D. Delmer, Sitosterol-beta-glucoside as primer for cellulose synthesis in plants. *Science* **295**, 147–150 (2002).
39. J. M. Jeckelmann, B., Transporters of glucose and other carbohydrates in bacteria. *Pflugers Arch.* **472**, 1129–1153 (2020).
40. E. Sajadi, V. Babaipour, A. A. Deldar, B. Yakhchali, S. S. A. Fatemi, Enhancement of crystallinity of cellulose produced by Escherichia coli through heterologous expression of bcsD gene from *Gluconacetobacter xylinus*. *Biotechnol. Lett.* **39**, 1395–1401 (2017).
41. G. Buldum, A. Bismarck, A. Mantalaris, Recombinant biosynthesis of bacterial cellulose in genetically modified *Escherichia coli*. *Bioprocess Biosyst. Eng.* **41**, 265–279 (2018).
42. S. S. Al-Janabi, H. Shawky, A. A. El-Waseif, A. A. Farrag, T. M. Abdelghany, D. E. El-Ghwas, Stable, efficient, and cost-effective system for the biosynthesis of recombinant bacterial cellulose in *Escherichia coli* DH5α platform. *J. Genet. Eng. Biotechnol.* **20**, 90 (2022).
43. M. Florea, H. Hagemann, G. Santosa, J. Abbott, C. N. Micklem, X. Spencer-Milnes, L. de Arroyo Garcia, D. Paschou, C. Lazenbatt, D. Kong, H. Chughtai, K. Jensen, P. S. Freemont, R. Kitney, B. Reeve, T. Ellis, Engineering control of bacterial cellulose production using a genetic toolkit and a new cellulose-producing strain. *Proc. Natl. Acad. Sci. U.S.A.* **113**, E3431–E3440 (2016).
44. M. Schramm, S. Hestrin, Factors affecting production of cellulose at the air/liquid interface of a culture of *Acetobacter xylinum*. *J. Gen. Microbiol.* **11**, 123–129 (1954).
45. I. Altinoglu, G. Abriat, A. Carreaux, L. Torres-Sánchez, M. Poidevin, P. V. Krasteva, Y. Yamaichi, Analysis of HubP-dependent cell pole protein targeting in *Vibrio cholerae* uncovers novel motility regulators. *PLOS Genet.* **18**, e1009991 (2022).
46. S. Zouhir, W. Abidi, M. Caleechurn, P. V. Krasteva, Structure and multitasking of the c-di-GMP-sensing cellulose secretion regulator BcsE. *MBio* **11**, (2020).
47. K. Zhang, Gctf: Real-time CTF determination and correction. *J. Struct. Biol.* **193**, 1–12 (2016).
48. A. Punjani, J. L. Rubinstein, D. J. Fleet, M. A. Brubaker, cryoSPARC: Algorithms for rapid unsupervised cryo-EM structure determination. *Nat. Methods* **14**, 290–296 (2017).
49. S. Q. Zheng, E. Palovcak, J. P. Armache, K. A. Verba, Y. Cheng, D. A. Agard, MotionCor2: Anisotropic correction of beam-induced motion for improved cryo-electron microscopy. *Nat. Methods* **14**, 331–332 (2017).
50. P. Emsley, B. Lohkamp, W. G. Scott, K. Cowtan, Features and development of Coot. *Acta Crystallogr. D Biol. Crystallogr.* **66**, 486–501 (2010).
51. P. D. Adams, P. V. Afonine, G. Bunkóczi, V. B. Chen, I. W. Davis, N. Echols, J. J. Headd, L. W. Hung, G. J. Kapral, R. W. Grosse-Kunstleve, A. J. McCoy, N. W. Moriarty, R. Oeffner, R. J. Read, D. C. Richardson, J. S. Richardson, T. C. Terwilliger, P. H. Zwart, PHENIX: A comprehensive Python-based system for macromolecular structure solution. *Acta Crystallogr. D Biol. Crystallogr.* **66**, 213–221 (2010).
52. R. T. Kidmose, J. Juhl, P. Nissen, T. Boesen, J. L. Karlsen, B. P. Pedersen, *Namdinator*—Automatic molecular dynamics flexible fitting of structural models into cryo-EM and crystallography experimental maps. *IUCrJ* **6**, 526–531 (2019).
53. E. Kandiah, T. Giraud, A. de Maria Antolinos, F. Dobias, G. Effantin, D. Flot, M. Hons, G. Schoehn, J. Susini, O. Svensson, G. A. Leonard, C. Mueller-Dieckmann, CM01: A facility for cryo-electron microscopy at the European Synchrotron. *Acta Crystallogr. D Struct. Biol.* **75**, 528–535 (2019).

54. S. F. Altschul, T. L. Madden, A. A. Schäffer, J. Zhang, Z. Zhang, W. Miller, D. J. Lipman, Gapped BLAST and PSI-BLAST: A new generation of protein database search programs. *Nucleic Acids Res.* **25**, 3389–3402 (1997).
55. L. A. Kelley, S. Mezulis, C. M. Yates, M. N. Wass, M. J. E. Sternberg, The Phyre2 web portal for protein modeling, prediction and analysis. *Nat. Protoc.* **10**, 845–858 (2015).
56. D. E. Kim, D. Chivian, D. Baker, Protein structure prediction and analysis using the Robetta server. *Nucleic Acids Res.* **32**, W526–W531 (2004).
57. M. Baek, F. DiMaio, I. Anishchenko, J. Dauparas, S. Ovchinnikov, G. R. Lee, J. Wang, Q. Cong, L. N. Kinch, R. D. Schaeffer, C. Millán, H. Park, C. Adams, C. R. Glassman, A. DeGiovanni, J. H. Pereira, A. V. Rodrigues, A. A. van Dijk, A. C. Ebrecht, D. J. Opperman, T. Sagmeister, C. Buhlheller, T. Pavkov-Keller, M. K. Rathinaswamy, U. Dalwadi, C. K. Yip, J. E. Burke, K. C. Garcia, N. V. Grishin, P. D. Adams, R. J. Read, D. Baker, Accurate prediction of protein structures and interactions using a three-track neural network. *Science* **373**, 871–876 (2021).
58. J. Jumper, R. Evans, A. Pritzel, T. Green, M. Figurnov, O. Ronneberger, K. Tunyasuvunakool, R. Bates, A. Žídek, A. Potapenko, A. Bridgland, C. Meyer, S. A. A. Kohl, A. J. Ballard, A. Cowie, B. Romera-Paredes, S. Nikolov, R. Jain, J. Adler, T. Back, S. Petersen, D. Reiman, E. Clancy, M. Zielinski, M. Steinegger, M. Pacholska, T. Berghammer, S. Bodenstein, D. Silver, O. Vinyals, A. W. Senior, K. Kavukcuoglu, P. Kohli, D. Hassabis, Highly accurate protein structure prediction with AlphaFold. *Nature* **596**, 583–589 (2021).
59. F. Sievers, A. Wilm, D. Dineen, T. J. Gibson, K. Karplus, W. Li, R. Lopez, H. McWilliam, M. Remmert, J. Söding, J. D. Thompson, D. G. Higgins, Fast, scalable generation of high-quality protein multiple sequence alignments using Clustal Omega. *Mol. Syst. Biol.* **7**, 539 (2011).
60. A. M. Waterhouse, J. B. Procter, D. M. Martin, M. Clamp, G. J. Barton, Jalview version 2—A multiple sequence alignment editor and analysis workbench. *Bioinformatics* **25**, 1189–1191 (2009).
61. L. Holm, Benchmarking fold detection by DaliLite v.5. *Bioinformatics* **35**, 5326–5327 (2019).
62. E. Krissinel, K. Henrick, Inference of macromolecular assemblies from crystalline state. *J. Mol. Biol.* **372**, 774–797 (2007).
63. N. R. Voss, M. Gerstein, 3V: Cavity, channel and cleft volume calculator and extractor. *Nucleic Acids Res.* **38**, W555–W562 (2010).
64. R. A. Laskowski, J. Jabłońska, L. Pravda, R. S. Vařeková, J. M. Thornton, PDBsum: Structural summaries of PDB entries. *Protein Sci.* **27**, 129–134 (2018).
65. E. F. Pettersen, T. D. Goddard, C. C. Huang, G. S. Couch, D. M. Greenblatt, E. C. Meng, T. E. Ferrin, UCSF Chimera—A visualization system for exploratory research and analysis. *J. Comput. Chem.* **25**, 1605–1612 (2004).
66. E. F. Pettersen, T. D. Goddard, C. C. Huang, E. C. Meng, G. S. Couch, T. I. Croll, J. H. Morris, T. E. Ferrin, UCSF ChimeraX: Structure visualization for researchers, educators, and developers. *Protein Sci.* **30**, 70–82 (2021).

Acknowledgments: We are grateful to all current and former members of the SBB group and especially to A. Siroy for useful discussions; Y. Yamaichi, D. H. Coucheron, and K. Tajima for providing bacterial strains; members of the Fronzes and Hashem laboratories for technical discussions; and E. Kandiah and M. Hons for CM01 data collection assistance. **Funding:** This project received funding from the ERC Executive Agency under grant agreement 757507 —BioMatrix-ERC-2017-StG (to P.V.K.) and was also supported by the IECB, the CNRS, and a Université de Bordeaux IDEX Junior Chair grant (to P.V.K.). The work has also supported and benefited from the IECB cryo-EM platform, and we acknowledge the European Synchrotron Radiation Facility for provision of beam time on CM01. J.-M.G. and S.L. were supported by the Laboratoire d'Excellence "Integrative Biology of Emerging Infectious Diseases" (grant ANR-10-LABX-62-IBEID). **Author contributions:** P.V.K. conceived the project. P.V.K., W.A., M.D., L.T.-S., and L.P. designed, performed, and optimized the experimental procedures. P.V.K., W.A., M.D., and L.T.-S. analyzed the data, and P.V.K. wrote the paper with contributions from L.T.-S., M.D., and L.P. and feedback from all authors. S.L. and J.-M.G. provided the pSEVA331Bb plasmid, raised and benchmarked the anti-BcsD antibody, and contributed to stimulating discussions. **Competing interests:** The authors declare that they have no competing interests. **Data and materials availability:** All data needed to evaluate the conclusions in the paper are present in the paper and/or the Supplementary Materials. Refined structural models and electron density maps have been deposited in the electron microscopy (emd-15039, emd-15040, and emd-15041) and protein databanks (pdb-7ZZQ and pdb-7ZZY).

Submitted 26 May 2022
Accepted 17 November 2022
Published 16 December 2022
10.1126/sciadv.add1170